Microstructural Characterization of SUS 444 Ferritic Stainless Steel

Nana Kwame Gyan Yamoah

Thesis submitted to the faculty of the Virginia Polytechnic Institute and State University in partial fulfillment of the requirements for the degree of

Master of Science In
Materials Science and Engineering

Mitsuhiro Murayama, Committee Chair
William T. Reynolds, Member
Alan P. Druschitz, Member

April 26th, 2013
Blacksburg, Virginia

Keywords: High Temperature Strength, Laves Phase Precipitation, Dislocation Density, Continuous Recrystallization

Microstructural Characterization of SUS 444 Ferritic Stainless Steel

Nana Kwame Gyan Yamoah

Abstract

Redesigning heavy components with thinner components is one way to lower automotive weight and improve fuel efficiency. Therefore, replacing thick cast iron exhaust manifolds with thinner heat resistant stainless steel one is a prime example of this approach. Material for a thin exhaust manifold must tolerate cyclic thermal fatigue. In SUS 444, this characteristic is directly related to the influence of microstructure on high temperature strength and the stability of the microstructure at the high operating temperature range. The goal of this research is to identify the cause for the drastic difference in the stress-strain behavior between two potential manufacturer heat treatments that will serve as a simplified model case for high temperature cyclic fatigue. Transmission electron microscopy (TEM) based microstructure analyses of samples which have been aged at 750°C for 100 hours and then hot-tensile tested at 750°C with a strain rate of $5 \times 10^{-5}/sec$ suggest continuous recrystallization as the mechanism responsible for the stable high temperature strength. The initial high temperature strength observed in the unaged sample was due to the precipitation of fine Laves phases which pinned down the motion of dislocations. As deformation progressed the strength increased until a critical precipitate size, volume fraction and dislocation density before Laves phases begun to rapidly coarsen and resulted in the abrupt decrease in strength. Microstructure evidence suggests the absence of precipitation strengthening effect in the aged samples could be a contributing factor to the decrease in peak strength between the aged samples and the unaged samples.

Acknowledgement

I would like to acknowledge my family for all the support and encouragement given me throughout my education. I would also like to thank my advisor Dr. Mitsuhiro Murayama and my committee members, Dr. William Reynolds and Dr. Alan Druschitz for their patience and guidance during my study. Dr. Jun Ichi Hamada was very helpful in providing samples and conducting the mechanical tests needed in my work.

I appreciate the time Dr. Niven Monsegue put in to train me on the TEM and his valuable input in this work. Financially, Nippon Steel and Sumikin Stainless Steel were of tremendous help. Finally, I am grateful to NCFL for the use of their laboratory facility during this work.

Table of Contents

List of Figures

List of Tables

1 CHAPTER 1 – INTRODUCTION

In an attempt to prevent environmental pollution and also to improve the efficiency of automobile, thin sheets and pipes of ferritic stainless steel are being used for the exhaust systems of automobiles instead of conventional cast iron which was previously used for this application [1]. By reducing the thickness of the exhaust system material, the thermal capacity is greatly decreased for cleaner exhaust gas to be released at a higher temperature, usually 900℃ [1, 2]. This technique also results in weight savings and better fuel economy.

The hot and cold ends make up the exhaust system. The hot end consist of the following components; exhaust manifold, front pipe, flexible pipe and catalytic converter and the cold end is made up of a center pipe, main muffler and tail end pipe (Figure 1.1). The current materials used for an exhaust system components and the typical operating temperatures are shown in Table 1.1. The high operating temperatures and the sporadic heating and cooling cycles of the exhaust system may cause buckling which results in thermal strain concentration at the point of buckling which eventually leads to fracture [3, 4]. Thus, materials for automobile exhaust systems require high temperature strength as well as excellent thermal fatigue resistance.

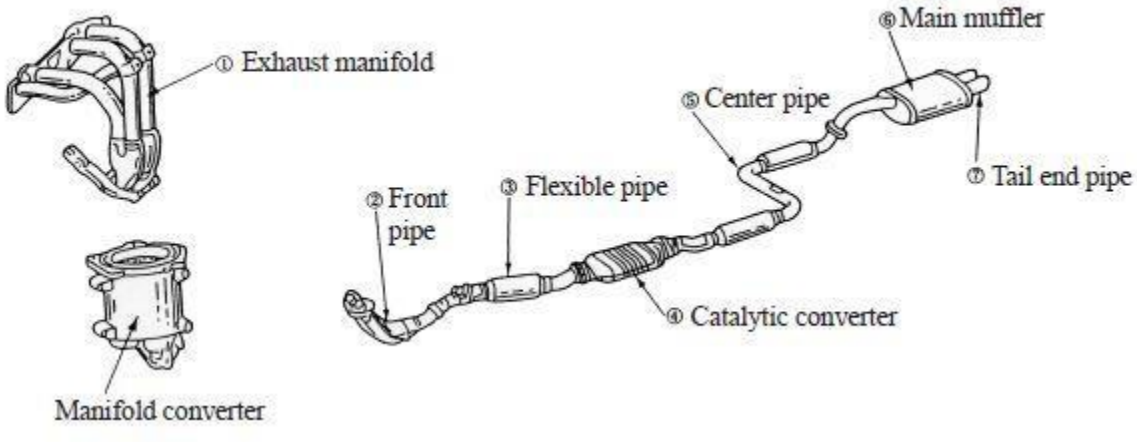

Figure 1.1. Automobile exhaust system components [5]

Table 1.1. Components of automobile exhaust system and their typical operating temperatures [5-7]

<table>
<tr><th colspan="2">Component</th><th>Service temperature (℃)</th><th>Required properties</th><th>Current materials</th></tr>
<tr><td colspan="2">Exhaust manifold</td><td>950 - 750</td><td rowspan="3">• High temperature strength
• Thermal fatigue life
• Oxidation resistance
• Workability</td><td>409, 441, 304, 321, 309</td></tr>
<tr><td colspan="2">Front pipe</td><td rowspan="3">800 - 600</td><td>304, 321, 309, 409</td></tr>
<tr><td colspan="2">Flexible pipe</td><td>304, 321, 309 and 316 Ti</td></tr>
<tr><td rowspan="2">Catalytic converter</td><td>Shell</td><td>• High temperature strength
• High temperature salt damage resistance
• Workability</td><td rowspan="2">441, 409, 321, 309</td></tr>
<tr><td>Catalyst carrier</td><td>1000 - 1200</td><td>• Oxidation resistance
• Thermal shock resistance</td></tr>
<tr><td colspan="2">Center pipe</td><td>600 - 400</td><td>• Salt damage resistance</td><td>304, 409, 441</td></tr>
<tr><td colspan="2">Main muffler</td><td rowspan="2">400-100</td><td rowspan="2">• Corrosion resistance at inner surface
• Corrosion resistance at outer surface</td><td>409, 434, 436, 430 Ti, 321, 304</td></tr>
<tr><td colspan="2">Tail end pipe</td><td>304, 316</td></tr>
</table>

Generally, austenitic steels have higher strength at high temperature than ferritic stainless steels but a lower thermal fatigue resistance compared to ferritic stainless steels. For example, type 304, a typical austenitic stainless steel, has lower thermal fatigue resistance than type 430 ferritic stainless steels [8]. This is because austenitic stainless steels have higher coefficient of thermal expansion than ferritic stainless steels. Austenitic stainless steels are also rather very expensive compared to ferritic stainless steels. Therefore, ferritic stainless steels are the commonly used materials in exhaust systems as a compromise between inexpensive carbon steels and the higher cost of higher alloyed ferritic or austenitic stainless steels. However, efforts must be made to improve its high temperature strength. In this regard, a lot of research is currently on-going for the development of a ferritic stainless steel with high temperature strength to complement its

superior thermal fatigue resistance [8-12]. Nippon Steel, in efforts to study the high temperature strength of ferritic stainless steel conducted high temperature tensile tests on SUS 444, a type of Nb-Ti-Mo stabilized ferritic stainless steel. The testing conditions were chosen to simulate the normal operating conditions of an exhaust manifold during service. They found that, the as-fabricated SUS 444 possesses initial excellent high temperature strength but its strength decreased rapidly as the strain was increased. However, after aging at 750℃ for 100 hours the initial high temperature strength decreased by more than half but rather, the aging treatment proved useful for stabilizing strength (Figure 1.2).

This work seeks to understand the differences in the stress – strain behavior of the as-fabricated and aged SUS 444 by studying their microstructures to determine the effects of the hot tensile testing conditions on the high temperature strength of SUS 444. This will ultimately provide more insight on the evolution of the microstructure of exhaust manifold during service.

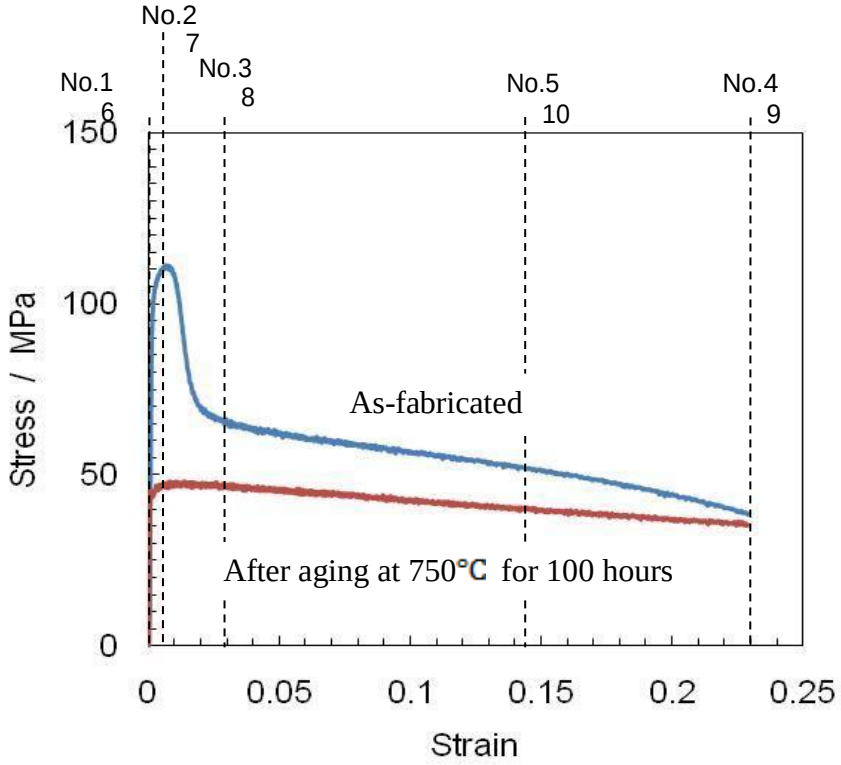

Figure 1.2. Stress - strain behavior of SUS 444 at 750℃.

2 CHAPTER 2 – BACKGROUND

2.1 High temperature strength ferritic stainless steels

A material for an exhaust manifold must tolerate cyclic thermal fatigue because of the repeatedly heating and cooling cycles due to vehicle operation. Nb uniformly dispersed in the ferrite matrix as an alloying element increases the initial high temperature strength compared to other alloying elements as shown in Figure 2.1 [8]. Fujita et al. also reported the effect of combined addition of Nb and Mo in a 0.01C - 0.01N - 13Cr steel on the 0.2% proof strength at 900℃ [13]. The addition of Nb is observed to be effective above 0.2 mass% Nb, however, Mo additions increases the high temperature strength proportionally to the alloy addition content, Figure 2.1 [13]. Therefore, Nb containing ferritic stainless steels are widely used in automotive exhaust systems because of their excellent high temperature strength, corrosion and thermal fatigue resistance. However, Nb is so reactive at high temperatures that that they form several types of precipitates during service, which can cause degradation in high temperature strength and thermal fatigue resistance [13].

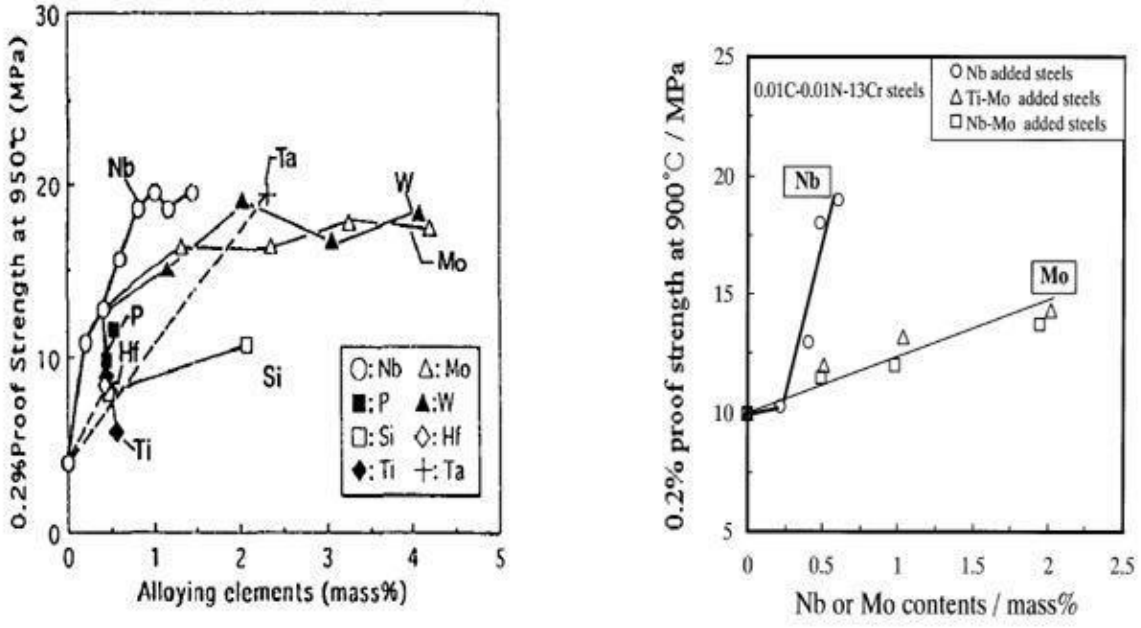

Figure 2.1. Effect of alloying element additions on the 0.2% proof strength at 900℃ of 13%Cr ferritic stainless steel [8, 13]. Reprinted from Fujita, N., et al., *Effect of Nb on high-temperature properties for ferritic stainless steel.* Scripta Materialia, 1996. **35**(6): p. 705-710 and Fujita, N., K. Ohmura, and A. Yamamoto, *Changes of microstructures and high temperature properties during high temperature service of Niobium added ferritic stainless steels.* Materials science & engineering. A, Structural materials: properties, microstructure and processing, 2003. **351**(1-2): p. 272-281, with permission from Elsevier [OR APPLICABLE SOCIETY COPYRIGHTT OWNER]

2.2 Factors affecting high temperature strength

Factors that affect high temperature strength of ferritic steels can be divided into two broad categories.

i. Formation, coarsening and dissolution of precipitates
ii. Recrystallization and recovery of the matrix grains

2.2.1 Formation, coarsening and dissolution of precipitates

The initial high temperature strength of niobium (Nb) – containing ferritic steels can be attributed to solid solution strengthening [8, 13]. Nb in the matrix reacts with carbon (C) and nitrogen (N) to form Nb containing precipitates during high temperature service. This is sometimes accompanied by the dissolution of metastable precipitates and the coarsening of stable precipitates and can be detrimental to the high temperature strength. Several types of precipitates are formed in Nb – containing steels during service, including Nb(C, N), Fe_3Nb_3C (M_6C) which are both cubic structure and Fe_2Nb (Laves phase) which has a hexagonal close packed structure.

Table 2.1. Crystallographic structure and the lattice parameters of precipitates found in Nb – containing ferritic steel [13].

Precipitate	Structure	Lattice parameter (nm)
NbC	Face-centered cubic	0.447
M_6C; Fe_3Nb_3C	Face-centered cubic	1.13
Laves; Fe_2Nb	Hexagonal	a = 0.482, c = 0.787

In the work done by Sawatani et al., they have shown that the precipitation rate of the Laves phase in a Ti and Nb stabilized steel reaches a maximum at 700℃ and its dissolution occurs at temperatures over 900℃ [14]. The Laves phase first precipitate

fine precipitates on sub- and grain boundaries as the steel is cooled from a high temperature of about 900℃. As the cooling rate becomes lower, the amount of Laves phase in the interior of grains increases and then those coarsened. In attempts to determine the solubility products in a niobium stabilized ferritic steel, it was found that a Mo addition as small as 0.5 mass% enhances the precipitation of Laves phase [13]. Murata et al, have also studied the dependence of the solvus temperature of the Laves phase on the alloying elements addition and have reported an increase in the solvus temperature with increasing alloying content [15].

Many authors have investigated the high temperature strength changes during high temperature aging of Nb added ferritic stainless steel [11, 13, 16]. It has been found that fine precipitates of Laves phase at grain boundaries improve the high temperature strength but the rapid coarsening of the Laves phase at high temperatures cancel out the beneficial effect [11]. To prevent the rapid coarsening of the Laves phase, the carbon content could be reduced drastically which may be difficult to do in the steel making process or other alloying elements such as Ti, Zr, Hf and Ta which have a strong affinity with C could be added [13, 17]. Sawatani et al studied the effect of Laves phase on the properties of Ti- and Nb stabilized low (C, N)-19%Cr-2%Mo stainless steel sheets and found that the Laves phase on the grain boundaries shifts the brittle to ductile transition temperature to a higher temperature [14]. They also observed that, large amounts of Laves phase precipitated after 20% cold rolled reduction, which results in an increase in strength and a decrease in elongation of the steel [14]. It was assumed that rapid increase in the amount of Laves phase precipitation could be due to an autocatalytic reaction as observed by Jones et al in Laves phase precipitation in Fe-Ta [18]. Cold working of approximately 20% is considered to give a high enough dislocation density to nucleate precipitates at dislocations, and also gives a low enough dislocation density to facilitate the formation of new dislocations due to the stress field created by precipitates [14]. The nucleation and growth of precipitates can best be explained by nucleation theories which will be discussed in the next section.

2.2.1.1 Homogeneous Nucleation

The total free energy change for homogenous nucleation can be represented as:

$$\Delta G = \frac{4}{3}\pi r^3 \Delta G_v + 4\pi r^2 \gamma + \frac{4}{3}\pi r^3 \Delta G_\varepsilon, \qquad \text{Equation 2.1}$$

Where ΔG_v is the Gibbs chemical free energy per unit volume of the new phase per unit volume and has a negative value, γ is the interfacial surface energy per unit area associated with the interface of the two phases and ΔG_ε is the misfit strain energy per unit volume. A plot of the total free energy equation demonstrates the dependency of the stability of the new embryo on its size, see Figure 2.2.

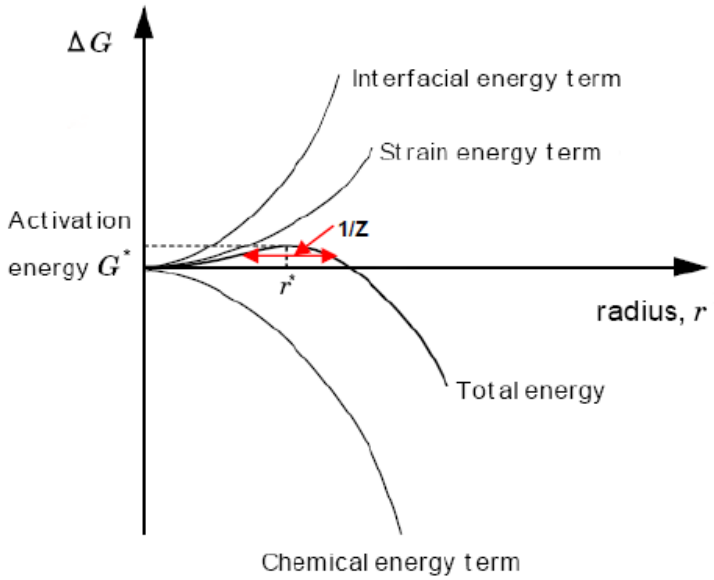

Figure 2.2. The free energy change associated with the formation of a stable nucleus with the radius [19]

The maximum total free energy occurs at a critical radius r^* when the free energy has a value ΔG^*, known as the activation energy. An embryo with a radius larger than r^* will grow spontaneously rather than dissolve since its growth leads to a decrease in free energy and then the embryo becomes a stable nucleus. At $r = r^*$, $d\Delta G/dr$ equals zero, so that ΔG^* is given by:

$$r^* = \frac{-2\gamma^2}{(\Delta G_v + \Delta G_\varepsilon)} \qquad \text{Equation 2.2}$$

$$\Delta G^* = \frac{16\pi\gamma^3}{3(\Delta G_v + \Delta G_\varepsilon)^2}$$ Equation 2.3

2.2.1.2 Heterogeneous Nucleation

The presence of impurity particles and structural defects such as dislocations and sub- and grain boundaries enable nuclei to be formed with a smaller free energy of activation than that of the homogeneous nuclei.

If we consider nucleation that takes place on a grain boundary, a certain surface area A of the grain boundary is removed from the system. This forms an additional driving force for nucleation and must, therefore have a negative sign in the basic free energy equation for nucleation, see the last term in Equation 2.4.

$$\Delta G = K_1\{\Delta G_v + \Delta G_\varepsilon\} + K_2\gamma_{ppt}A_{ppt} + K_3\gamma_{ppt/gb}A_{ppt/gb} - \gamma_{gb}A_{gb}$$

Equation 2.4

From this equation it is clear that the system will preferentially select higher energy grain boundary sites first where it will gain the most energy as an additional driving force. The relationship between the activation energy for grain boundary nucleation for the various possible grain boundary sites and the contact angle θ are shown in Figure 2.3. The ratio of the free energy required to form a grain boundary nucleus to that needed to form a homogeneous nucleus obviously decreases as the ratio of the grain boundary energy to the interphase boundary energy increases through the contact angle parameter cos θ.

From Figure 2.3 it can be seen that at a given contact angle θ, nucleation on grain corners requires the lowest activation energy, then grain edges and lastly grain boundaries. Grain boundaries can also lower the retarding force arising from the strain energy ΔG_ε and, thereby, create a new driving force. In cases where the surface energy and strain energy are lowered enough through nucleation on grain boundaries, the grain boundaries may become the preferred sites fully and no nucleation within the grains will occur. This is what is typically found in Al-Mg alloys where the β-phase nucleates only on grain boundaries and embrittles the alloy.

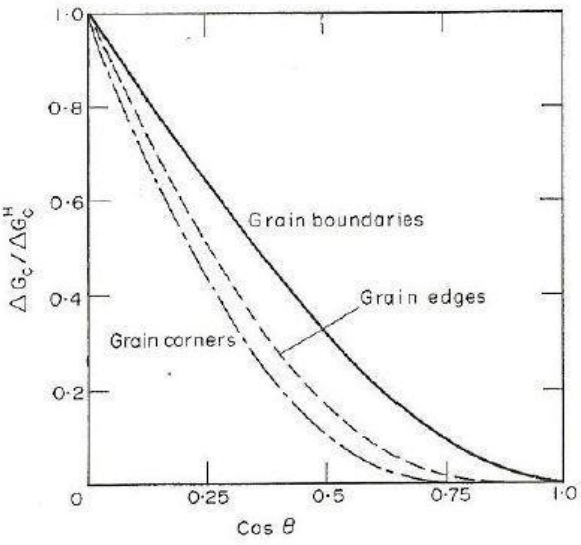

Figure 2.3. The ratio of the free energy required to form a nucleus on various types of grain boundary sites to that required to form a nucleus in the grain matrix, is plotted as a function of the contact angle parameter cos θ [19].

2.2.1.3 Coarsening

The coarsening rate of precipitates can be calculated using the classical theory of the Ostwald ripening equation that is due to Lifshitz and Slyozov, and Wagner and is often called LSW coarsening [20],[21].

$$r^3 - r_0^3 = \frac{8\gamma v^\beta D c^{\alpha\beta}}{9RT} t$$ Equation 2.5

Where r is the average particle radius, r_0 is the initial average particle radius, γ is the interfacial energy, D is the diffusion coefficient of the rate controlling species, v^β is the molar volume of the phase β, $c^{\alpha\beta}$ is the equilibrium solute concentration in the α matrix, r is the gas constant, T is the absolute temperature, t is the time at temperature.

2.2.2 Continuous and discontinuous recrystallization

Continuous recrystallization partially restores the grain structure of a deformed material to their initial properties prior to deformation and occur prior to discontinuous recrystallization. Continuous recrystallization depends on a number of parameters, including; crystal structure of the material, strain, strain rate, deformation temperature and annealing temperature [22]. The stacking fault energy affects the extent to which

dislocation dissociate and determines the rate of climb and cross slip. These are mechanisms which controls the rate of continuous recrystallization. In low stacking fault energy metals such as copper, $\alpha -$ brass and austenitic stainless steel, climb is difficult and little continuous recrystallization of the dislocation substructure occurs prior to discontinuous recrystallization. However in metals of high stacking fault energy such as aluminum and $\alpha -$ iron, climb is rapid and significant continuous recrystallization may occur [23]. The distinction between continuous and discontinuous recrystallization is sometimes difficult to define, because continuous recrystallization plays an important part in the subsequent discontinuous recrystallization. During continuous recrystallization the stored energy of the material is lowered by annihilation of dislocations and the rearrangement of dislocations into lower energy configurations by glide, climb and cross-slip of dislocations. Excess dislocations after dislocation annihilation will arrange into lower energy configuration in the form of low angle grain boundary (LAGBs) or subgrain, as schematically shown in Figure 2.4. Discontinuous recrystallization involves the subsequent conversion of the low angle grain boundary into high angle grain boundary, the process is shown in Figure 2.4.

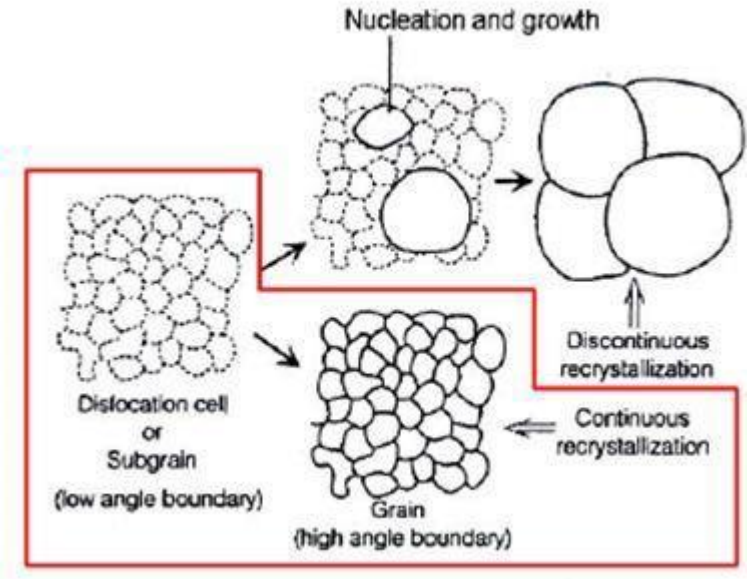

Figure 2.4. Continuous and Discontinuous recrystallization [24]

Nb is widely used as a microalloying element because it has a significant effect on the microstructure stability and mechanical properties of ferritic stainless steels. Depending on the state of Nb, whether in the matrix as solute or in precipitates, Nb affects the recrystallization kinetics and the grain growth [25]. The effect of Nb on the recrystallization kinetics and the grain growth of austenite has been widely studied [26]. Nb addition, even in small amounts, can lead to a significant decrease in grain boundary mobility, as well as an increase in the recrystallization temperature. Both the decrease in the grain boundary mobility and the increase in the recrystallization temperature can be attributed to the solute drag effect of Nb in the matrix and the pinning effect of fine precipitates such as NbC and Fe_2Nb. Suehiro has shown that Nb retards the migration of grain boundaries during recrystallization due to the solute drag effect [26]. His results show that Nb decreases the velocity of the recrystallization grain boundary at the composition covering the critical composition and this depends on the temperature and the total driving force. This retardation was found to be caused by the solute drag effect of Nb. Following this work, Suehiro et al. also studied the effect of Nb on the austenite to ferrite transformation in ultra-low carbon steel [27]. Their results indicate that there is a critical temperature where the rate of transformation changes drastically. The critical temperature was found to be composition dependent, and for 0.25% Nb alloy it was found to be 750℃ and for 0.75% Nb alloy it was 720℃. Schmitt has observed that depending on the temperature, a part of the precipitation occurs on the grain boundaries combined with a fine inter granular precipitation, and this strongly slows down the grain boundary mobility [28].

The rate of grain boundary movement proposed by Cahn, as it is affected by solute drag is [29]:

$$\frac{p_d}{v_b} = \frac{1}{M_T} = \frac{1}{M_0} + \frac{\alpha X_s}{(1+\beta^2 v_b^2)} \qquad \text{Equation 2.6}$$

Where p_d is the driving force for the grain boundary mobility and v_b is the mobility rate, M_T is the overall mobility due to intrinsic plus solute drag, M_0 is the intrinsic grain boundary mobility in pure material, X_s the atom fraction of solute in the bulk metal, α is a term related to the binding energy of solute to the grain boundary and β is a term related to the diffusivity of the solute in the vicinity of the grain boundary. It should also

be mentioned that the stored energy in a plastically deformed material may give rise to Strain Induced Boundary Migration (SIBM).

3 CHAPTER 3 – EXPERIMENTAL PROCEDURE

Table 3.1 shows the chemical composition of SUS444 received from Nippon Steel. Aging treatment was carried out at 750℃ for 100 hours to simulate the normal operating conditions of an automobile exhaust system.

Table 3.1. Chemical composition of SUS444 (mass %)

C	Si	Mn	P	S	Cr	Mo	Nb	Ti	N
0.005	0.35	0.99	0.03	0.001	18.4	1.8	0.48	0.10	0.012

3.1 Tensile Test

To evaluate the changes of microstructure and mechanical properties during high temperature service, high temperature tensile tests were carried out on both the as-cast samples and the aged samples in accordance with Japanese Industrial Standard. The high temperature tensile tests were carried out using dog bone type specimen at 750℃ at a strain rate of $5 \times 10^{-5}/sec$, see Figure 3.1.

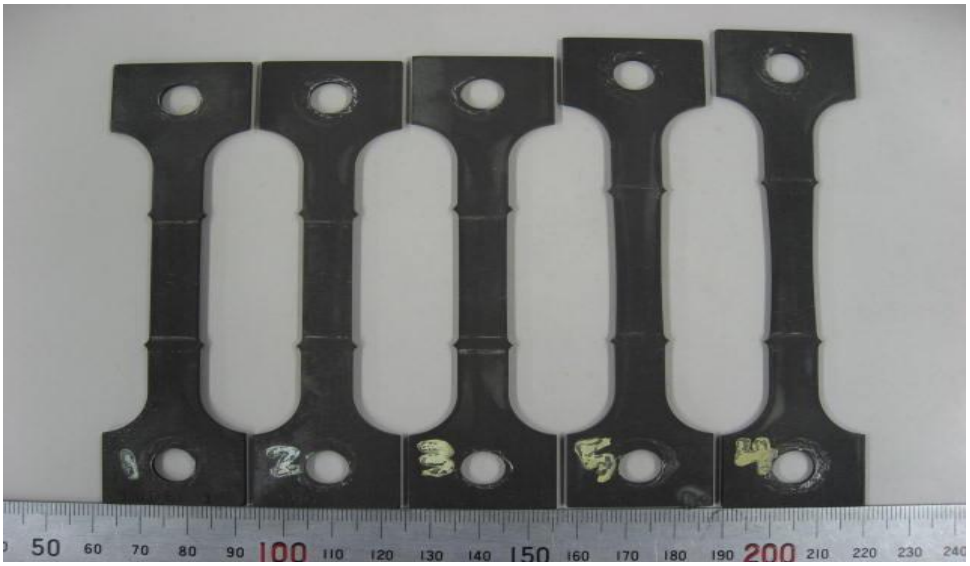

Figure 3.1. Dog bone type specimens after tensile test

3.2 Transmission Electron Microscopy (TEM)

3.2.1 Sample preparation

The cross section of the tensile test specimen is such that the grip has large shoulders so that they can be easily gripped and the gauge has a smaller cross section for deformation

and failure to easily occur in this area, see Figure 3.2. Samples were sectioned from the gage and the grip of the tensile tested specimens to compare the effect of strain on the microstructure of both the as-cast and aged specimens.

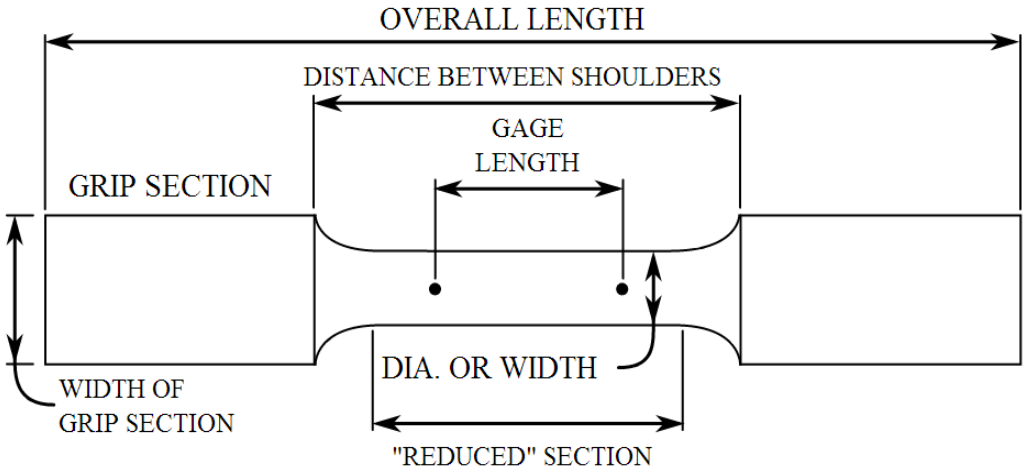

Figure 3.2. Cross section of a tensile test specimen

Samples were ground to 300um after which disks 3mm in diameter were punched and further polished to 50um. To reveal microstructure features, samples were electro-polished using a Fischione twin-jet M110 electro polisher. Optimum conditions to obtain electron transparent regions were obtained using a solution of 10% perchloric and 90% methanol at a temperature of $-50℃$, voltage of 10V and a current of 10mA.

3.2.2 Microstructural characterization

TEM foils were examined using a Philips EM420 microscope operating at 120kV. To observe the dislocation structure, it is important that all images are taken under the same imaging conditions as some dislocations become invisible in the TEM when g•b = 0. Therefore, series of bright field images were taken close to the [111] zone axis with a {111} reflection. The images were also taken at the same magnification so as to compare the microstructural features at the same sample area size. Selected Area Electron Diffraction (SAED) was used to identify the crystal structure of the precipitates in the samples. However, some of the precipitates were too small to be identified with the conventional SAED, therefore more complex technique such as nanodiffraction in the Scanning Transmission Microscopy (STEM) mode and Electron Dispersive X-ray Spectrometry (EDS) was carried out using the FEI Titan 300 operating at 300kV.

3.2.3 Microstructural analysis

Microstructural features were analyzed with image analysis tools such as Image J (NIH) and TEM Imaging and Analysis (TIA) software (FEI Company). To quantify the dislocation density in the TEM, two methods are generally used. The first method is by the measurement of the length of dislocation over unit volume. The second method requires the counting of the number of dislocation lines intersecting the surface over unit area. Several approaches to determine the thickness of TEM foils have been discussed by Williams and Carter [30]. Among them two approaches are relatively widely used: one utilizes the Kossel-Mollenstedt fringes in convergent beam electron diffraction (CBED) pattern and the second uses thickness fringes. However, the second method was used to quantify the dislocation density because of its simplicity.

The precipitate volume fraction was determined by superimposing a square grid over the microstructure and counting the points intersecting the precipitate over the total number of grid points. Grid points intersecting the interface of the precipitates were counted as half. This process was repeated for about thirty fields of views and the average found to be the volume fraction of precipitates. The precipitate size and grain size were measured with the help of Image J. Likewise several fields of views were analyzed.

3.3 Summary of Experimental Procedure

To determine the high temperature strength behavior of SUS 444, both as-cast and aged samples were hot tensile tested. TEM foils were made from the grip and gage parts of the tensile tested specimen by electropolishing. Parallel nano-beam electron diffraction in the Scanning Transmission Microscopy (STEM) mode and Electron Dispersive Spectrometry (EDS) was carried out using the FEI Titan 300 to identify small precipitates which could not be identified by SAED in the Philips EM420. Microstructural analysis was done with the help of Image J and TIA software.

4 CHAPTER 4 – RESULTS AND DISCUSSION

4.1 Introduction

This chapter examines collectively the experimental results. The main focus is to explain the stress-strain curves of unaged and aged SUS 444, see Figure 1.2. By so doing, the factors that affect the high temperature strength can be elucidated. To gain a better understanding of the factors that affect high temperature strength, the results are divided into three parts:

1. Identification of precipitates
2. The effect of testing time
3. The effect of strain

4.2 Identification of precipitates

In order to understand the stress-strain behavior of SUS 444 (Figure 1.2), microstructural analyses were carried out with the transmission electron microscope (TEM). It was however imperative to identify the precipitates by nanodiffraction in the scanning transmission electron microscope (STEM) mode and energy dispersive spectrometry (EDS). Figure 4.1 shows the scanning transmission electron micrographs and their analysis results of precipitates found in unaged SUS 444. Electron diffraction analysis identifies these precipitates to be Fe_2Nb type Laves phases. However, EDS analysis shows small amounts of chromium and Molybdenum to be included, therefore the composition of Fe_2Nb is most likely to be $(Fe, Cr)_2(Nb, Mo)$, see Figure 4.2. These Laves phases are thought to have formed during the high temperature testing as alloying elements supersaturated in the matrix precipitates out during testing. Figure 4.3 shows a STEM dark field (DF) micrograph of a triple junction in unaged SUS 444 showing Laves phase precipitates heavily decorated on two of the boundaries but nothing found on the third boundary. The micrograph in Figure 4.3 also shows precipitation on dislocations and almost none within the matrix. Therefore it is logical to assume that the nucleation of Laves phase occurs mainly on dislocations and then grain boundaries before they nucleate in the matrix. This assumption is consistent with the assumptions of the classical nucleation theory that nucleation first occurs at areas which requires the lowest activation energies for nucleation.

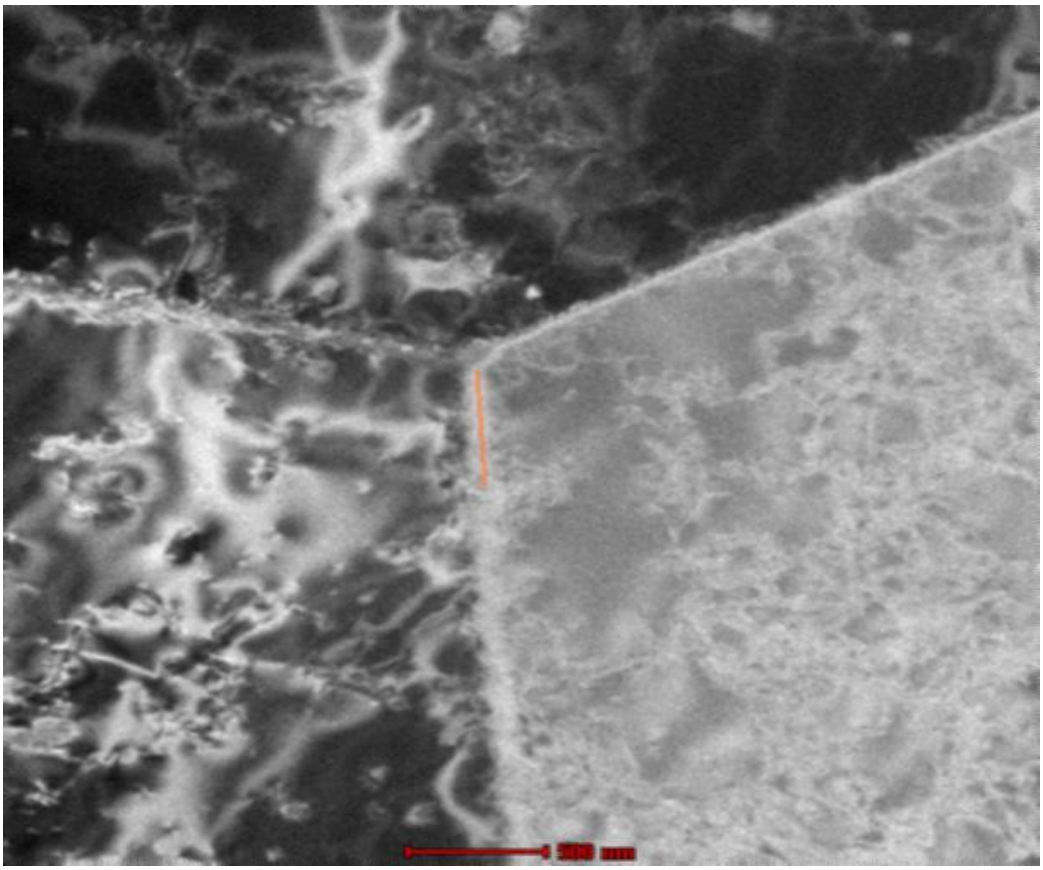

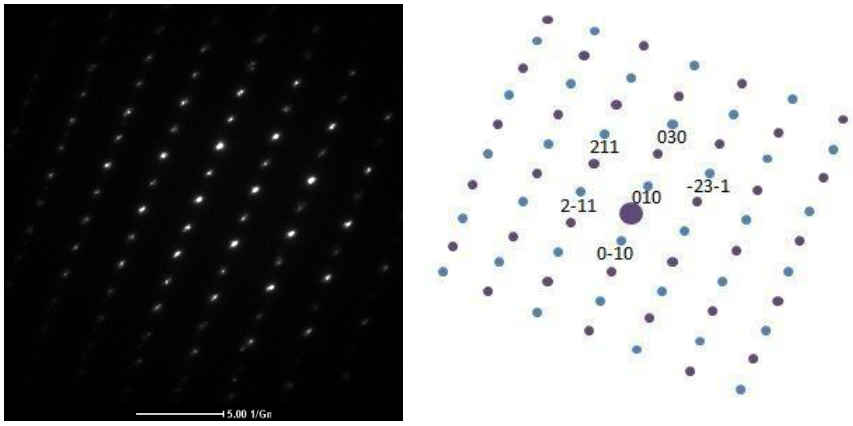

$$[111]_{matrix} // [10\bar{2}]_{Fe_2Nb}$$

Figure 4.1. Scanning transmission electron micrograph of Fe2Nb laves phase found on grain boundary in unaged SUS 444 and their analysis by electron diffraction

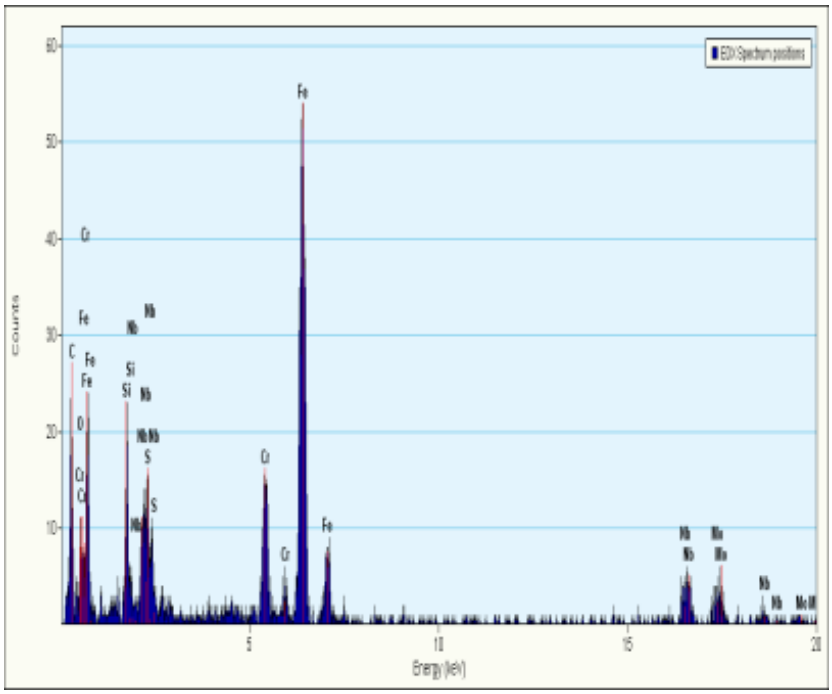

Figure 4.2 EDS analysis of Laves phase in SUS 444

Figure 4.3. STEM dark-field micrograph of Fe2Nb Laves phase precipitates found on a triple junction

Likewise, Fe_2Nb type Laves phase precipitates of different sizes and morphologies were identified in the aged samples. The morphologies of these Laves phases ranged from block-like, rod-like and small globular precipitates see Figure 4.3. Electron diffraction analysis of these precipitates indicates that all these precipitates are indeed Fe_2Nb laves phases. These precipitates are thought to have formed during aging at 750℃ for 100 hours. Sawatani et al. observed that the precipitation rate of the Laves phase in a Ti and Nb stabilized steel reached a maximum at 700℃ and its dissolution occurs at temperatures over 900℃ [14].

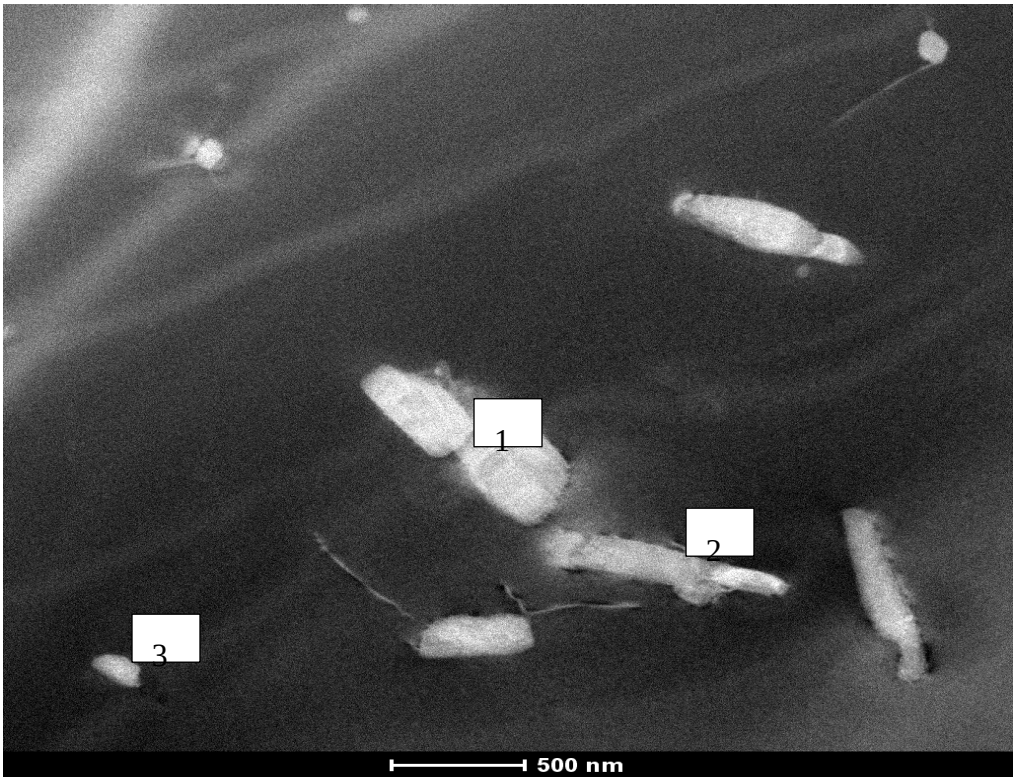

1. 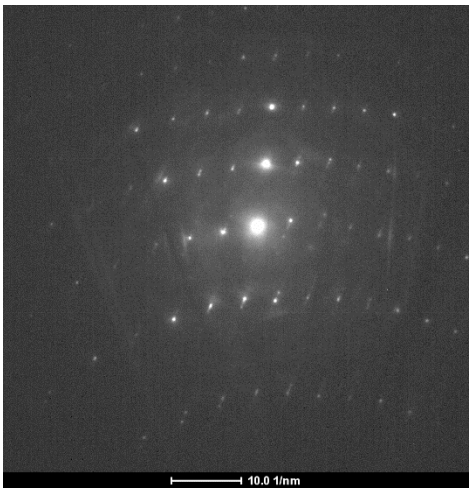

2. 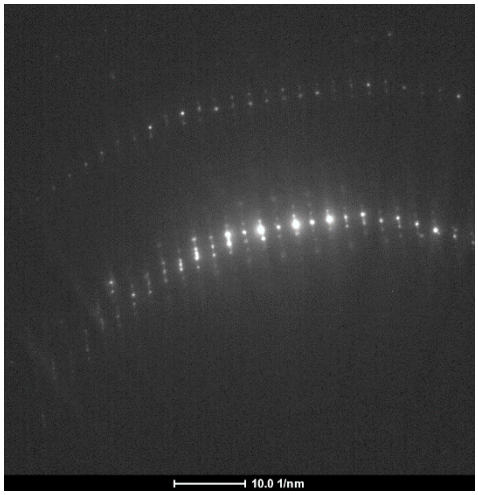

3. 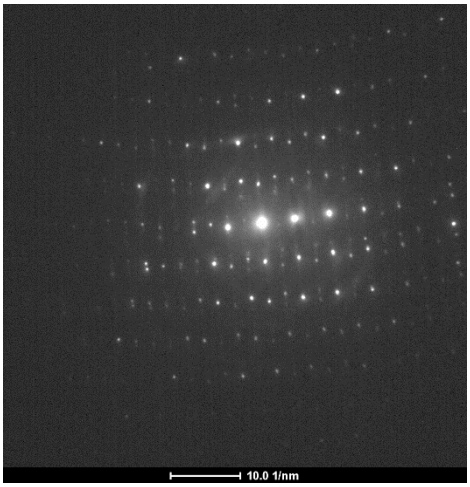

Figure 4.4. Scanning transmission electron micrographs of the different morphologies of Laves phase precipitates in aged SUS 444 and their analysis by electron diffraction.

4.3 The effect of testing time

In order to understand the behavior of the stress-strain curves of SUS 444, it is important to analyze the effect of testing time on its microstructure. The tensile test specimen is designed such that the grip does not take part in deformation, therefore any microstructural changes in the grip during testing can be solely attributed to the time spent during testing at the given temperature.

4.3.1 Unaged grip

Figure 4.5 shows the evolution of the microstructure of the unaged grip sample as the testing time is increased. At a strain rate of $5 \times 10^{-5}/sec$, it was determined that it took

approximately 1 minute at the testing temperature to undergo a strain of 0.3%. As can be seen from Figure 4.5, after testing at 750℃ for 1 minute, the microstructure has very few precipitates widely spaced over the entire area of the grain and a very clean grain boundary, suggesting that the testing time is too short to cause precipitation of laves phases. However, as the testing time is increased, the volume fraction of laves phase on the grain boundaries and in the matrix increase. After 47 minutes at the testing temperature, the volume fraction of precipitates increase as well as a much decorated grain boundary can be observed, see Figure 4.5. Miyazaki et al observed the precipitation of both Nb and Fe to reach a saturation after aging treatment at 700℃ for 2 hours in a 15%Cr – 0.5%Nb steel [31]. In Nb containing steels, the high temperature strength decreased steadily with increasing aging time despite minimal grain growth [11]. Therefore, the decrease in high temperature strength was attributed to loss of solid solution strengthening effect as the Nb present in the matrix goes into precipitates in the work done by Sim et al [11].

a) 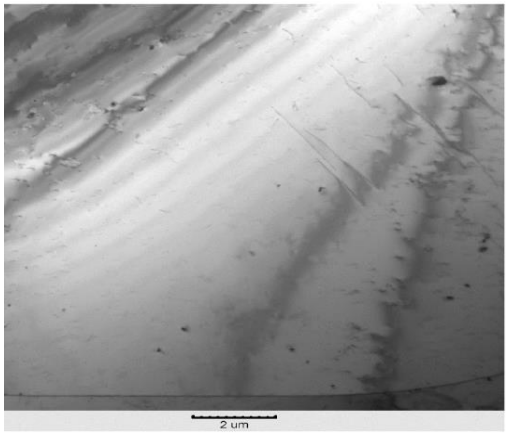

b) 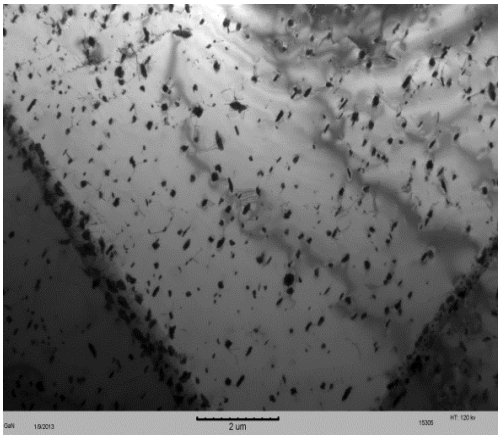

Figure 4.5. TEM micrograph of unaged grip SUS 444; a) microstructure of unaged grip after testing for 1 minute and b) microstructure after testing for 47 minutes

4.3.2 Aged grip

As expected, the microstructures of the aged grip samples did not show any significant difference with increase in testing time. The average precipitates size, average volume fraction of precipitates and distribution as well as the dislocation density did not show any markedly difference; see Figure 4.6 (a) and (b). As already pointed out, the testing

time was too short to cause further precipitation and coarsening of Laves phase after all the supersaturated alloying elements have already precipitated out during the aging treatment. Therefore, the microstructure of the aged grip sample is the representative microstructure of the as-aged samples.

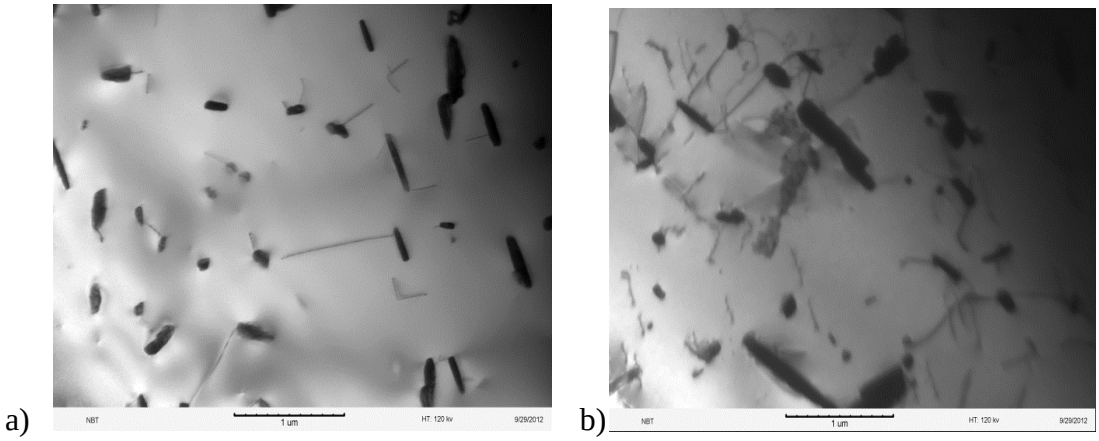

Figure 4.6. TEM micrograph of aged grip SUS 444; a) microstructure of aged grip after testing for 1 minute b) microstructure after testing for 47 minutes

4.4 The effect of strain

After analyzing the effect of testing time on the microstructure of grip specimens of SUS 444, the differences in microstructure between the grip and gauge samples can correctly be attributed to strain effect, and the behavior of the stress-strain curve can now be easily elucidated.

4.4.1 Unaged gauge

By critically observing the microstructure of the sample that has undergone a 0.3% strain, very small precipitates on the order of $\sim 20nm$ in diameter are seen to nucleate on dislocations, see Figure 4.7 (a). These Laves phases are thought to precipitate as a result of the deformation during the tensile test. Comparing this microstructure to the microstructure of the grip sample (Figure 4.5 (a)) shows that the grip sample had very few precipitates, therefore the presence of these precipitates on dislocations in the gauge must be strain induced. The sample deformed to 0.3% had the smallest particle size and

inter particle spacing so that they effectively pin the motion of dislocation and is responsible for the initial high temperature strength.

As the sample is deformed to 0.9%, the Laves phase precipitates coarsen and its volume fraction increases, see Figure 4.7 (b). The dislocation density also decreases, however, the strength rather increases, Figure 4.7 (b). This is fascinating because the microstructure of the sample strained to 0.3% is expected to have the highest strength since it has the finest Laves phase precipitates. The dislocation density in the sample strained to 0.3% also has the highest dislocation density and it is expected that the dislocations will obstruct each other's movement and result in the highest strength. This is however not the case, the sample deformed to 0.9% rather has the highest strength. In the work by Haitao et al. the strength of 11Cr-0.2Ti-0.4Nb ferritic stainless steel aged at 800℃ increased with increasing aging time from 24 hours to 48 hours even though the average size of precipitates increased but increasing the aging time to 96 hours at 800℃ resulted in the further coarsening of precipitates which led to a decrease in strength [16]. Therefore, it can be inferred that there is a critical average size of Laves phase precipitates to achieve the maximum strength beyond which the strength decreases. This assumption can be extended to the dislocation density as well since the sample strained to 0.9% has the lowest dislocation density but it has the highest strength amongst all three samples analyzed.

In Figure 4.7 (c), deformation to 3.0% resulted in further coarsening of Laves phase precipitates and led to a decrease in strength which is in agreement with the observation made by Sim et al where fine precipitate of Laves phase improved the high temperature strength of Nb – containing steels when still fine but rapid coarsening of the Laves phase at high temperatures decreased the high temperature strength [11]. Though there is a decrease in dislocation density, the coarsening of the Laves phase and the increase in inter particle spacing suggests that the pinning effect of the Laves phase precipitates is compromised and may also contribute to the decreased strength. Also, block-like Laves phase precipitates were observed in the unaged sample strained to 3.0% which were not observed in the other unaged samples analyzed. Therefore, it can be inferred that the block-like Laves phase precipitates may have contributed to the decreased strength.

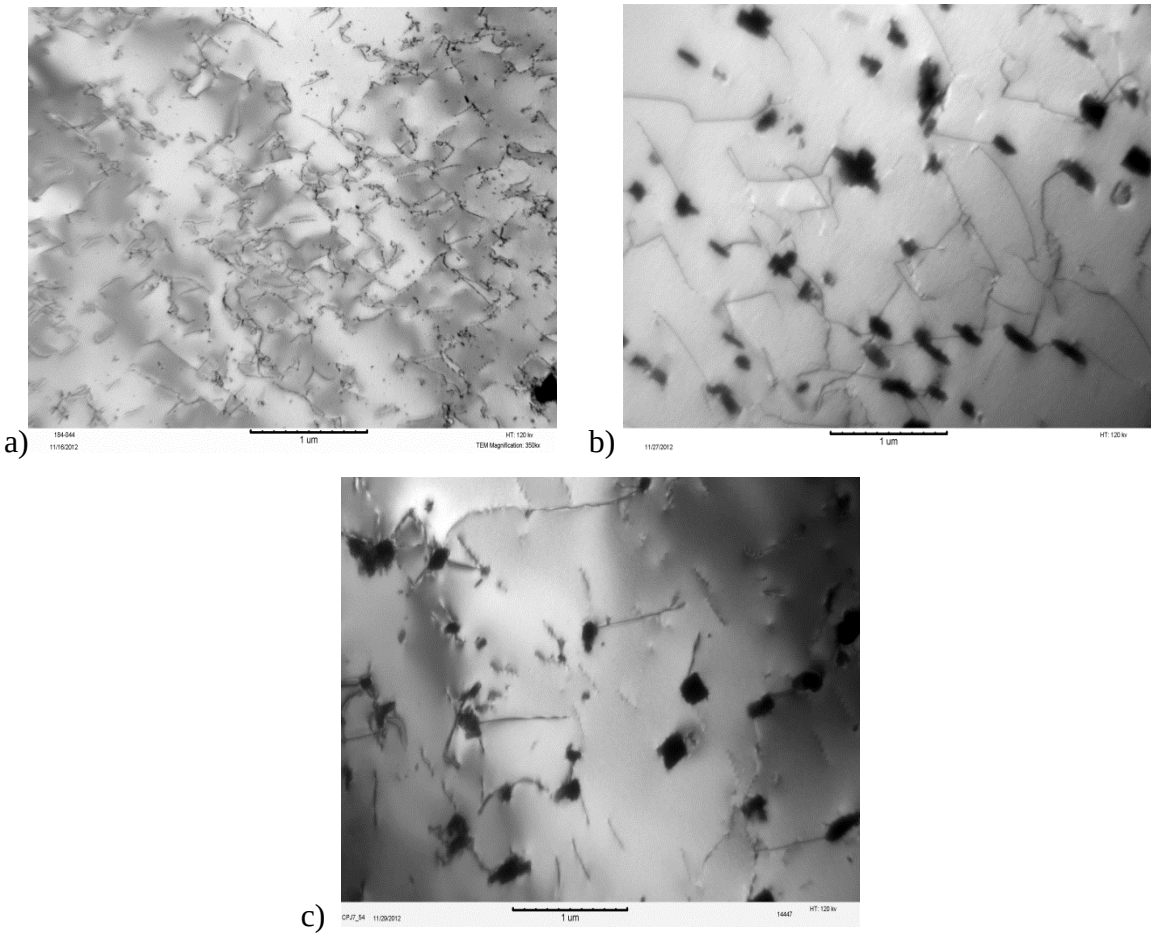

Figure 4.7. TEM micrographs of unaged gauge SUS 444; a) strain induced precipitation of laves phase after 0.3% strain b) coarsening of precipitates after a strain of 0.9% c) precipitates continues to coarsen and volume fraction decreases after a strain of 3.0%

4.4.2 Aged gauge

In the aged gauge samples, the microstructure of the sample that has undergone a 0.3% strain shows a microstructure consisting of dislocation tangles and the highest dislocation density, as seen in Figure 4.8 (a). The presence of the dislocation tangles decreases the average distance between dislocations and the dislocations start to block the motion of each other, therefore the initial high strength observed after deformation to 0.3%. As deformation continues, continuous recrystallization occurs but no evidence of discontinuous recrystallization was observed because of the low strains used in this work. Tsuzaki et al studied the microstructural evolution during the superplastic deformation in

a microduplex stainless steel and found continuous recrystallization to be the dominant mechanism in the early stages of deformation [32]. In the continuous recrystallization process, grain boundaries absorb dislocations and dislocations with opposite signs annihilate to form a lower dislocation density inside the grain. This process is accompanied simultaneously by the formation of serrated boundaries which form a dislocation wall (or subgrain boundary) as seen in Figure 4.8 (b). Further deformations up to a strain of 14.3% shows the serrated boundaries have converted into a subgrain structure; see Figure 4.8 (c). In Figure 4.9, the strain field originating from the precipitates on the grain boundary shows only a slight misorientation as it passes through successive grains indicating that the grains are only separated by a low angle boundary (LAB) and so confirming its subgrain structure. From the above observation, it can be inferred that sub grains are first formed in the vicinity of the serrated grain boundaries (cell walls) which are formed as a result of dislocation absorption on grain boundaries and dislocation annihilation and as deformation progresses, sub grain structure will form over the whole volume of the grain through the conversion of dislocation cell walls into sub grain structure with low angle boundaries.

a) 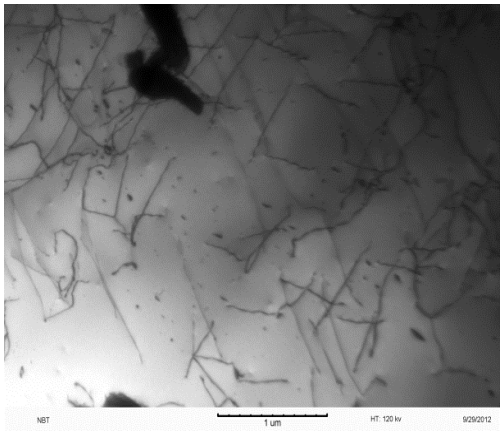

b) 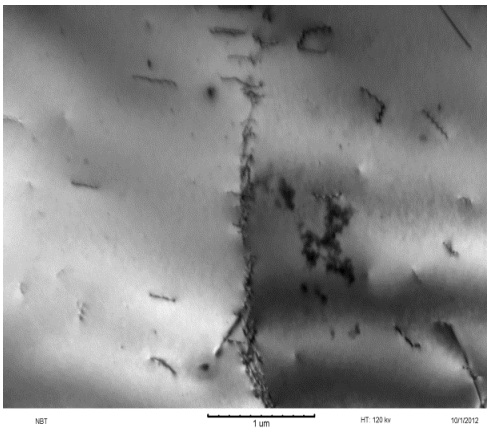

c) 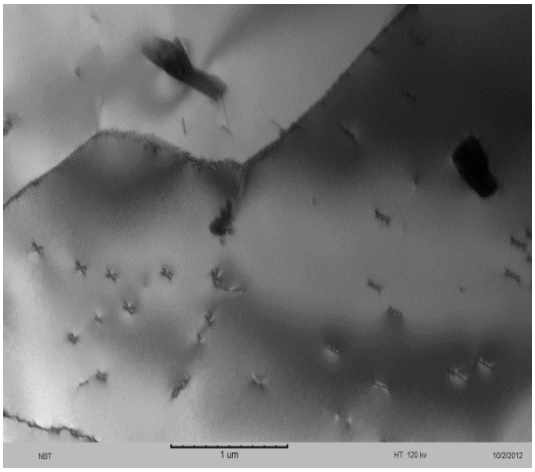

Figure 4.8. TEM micrographs of aged gauge SUS 444; a) dislocation tangles after a strain of 0.3% b) serrated boundary with lower dislocation density after a strain of 3.0% c) subgrain structure after a strain of 14.3%.

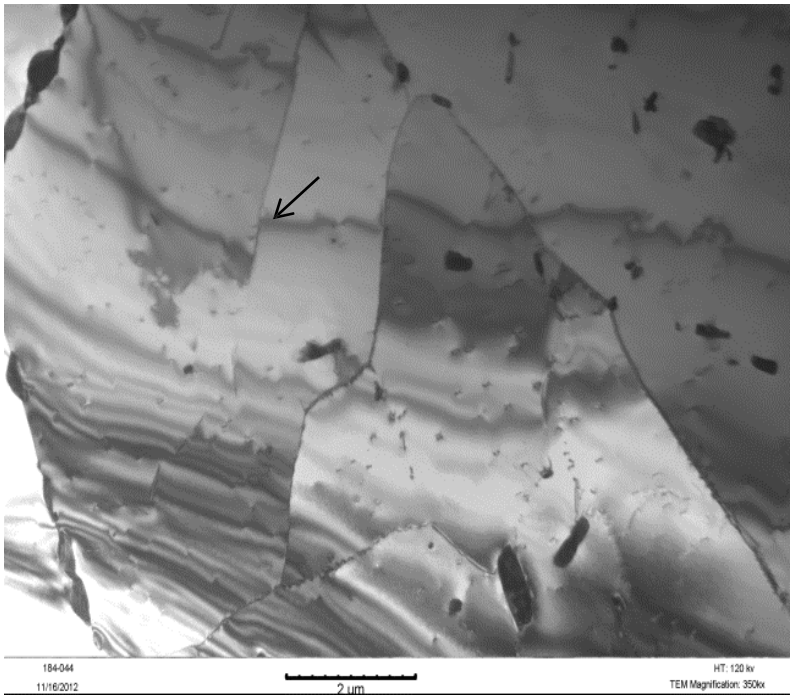

Figure 4.9. Low magnification image of aged gauge SUS deformed to a strain of 14.3% showing low angle boundaries as depicted by the strain field originating from the precipitate on the grain boundary

5 CHAPTER 5 – CONCLUSION

The microstructures of unaged and aged SUS 444 ferritic stainless steel have been analyzed with the TEM to determine the factors that affect high temperature strength of SUS 444. The following may be concluded:

1. Strain induced precipitation of fine Laves phase was observed in the unaged sample deformed to 0.3%. The sample strained to 0.3% had the shortest inter particle spacing ensuring that they effectively pin the motion of dislocation and is responsible for the initial high temperature strength.
2. Laves phase coarsens and dislocation density decreases after further deformation to 0.9%, however the strength rather increases. The mechanism responsible for the increase in strength is not very clear, however, the evidence suggest there is a potential critical size and volume fraction of laves phase, dislocation density etc. to achieve the optimum strength.
3. At 3.0% strain, the dislocation density increased but the further coarsening of the Laves phase and the increase in inter particle spacing decreased the effectiveness of dislocation pinning, hence the decrease in strength. Also, the precipitation of block-like Laves phase could also be responsible for the decrease in strength.
4. The decrease in peak strength after aging at 750℃ for 100 hours could be as a result of several thriving mechanisms. Many researchers have attributed the decrease in strength after aging in this temperature range to the loss of solid solution strengthening effect, however, the drastic increase in size of the Laves phase as well as the increase in inter particle spacing suggest the loss of precipitation strengthening could be a contributing factor to the decreased strength. Also, the change in morphology of the Laves phases precipitates from the initial globular precipitates in the unaged samples to mostly rod-like precipitates after aging could possibly be a factor in the decreased strength after aging.
5. A high dislocation density comprising of dislocation tangles characterized the aged sample deformed to 0.3%. The presence of dislocation tangles impedes the motion of the dislocations and results in the initial high strength.

6. Dislocation annihilation and rearrangement into a low energy configuration to form dislocation cell walls as the sample was strained to 3.0% decreased the strength only slightly since dislocation motion is now enhanced.
7. Further deformation to 14.3% resulted in the conversion of dislocation cell walls into subgrains with low angle boundaries.
8. The Laves phase average sizes, volume fraction and inter particle spacing in all the aged samples did not differ significantly. Therefore the microstructural changes in the aged samples are consistent with continuous recrystallization.

REFERENCES

1. Honma, M., Jidosha-gijutsu Society of Automotive Engineering of Japan, Inc., 1989. **43**: p. 55.
2. Gallo S., M.C., Nicodemi W. and Pontimi G, in *Pro. 3rd Eur. Cong. on Stainless Steel '99*1999: Milan. p. 95.
3. Oku, M., CAMP-ISIJ, 1991. **4**: p. 1793.
4. Yamanaka M., et al., Seitetsu-Kenkyu, 1983. **311**: p. 33–39.
5. Inoue Y. and Kikuchi M., *Present and future of stainless steel for automotive exhaust system.* Nippon Steel Technical Report, 2003. **88**: p. 62-69.
6. Sato Eiji and Tanoue Toshio, *Present and future trends of materials for automotive exhaust system.* Nippon Steel Technical Report, 1995(Journal Article).
7. Miyazaki, A., K. Takao, and O. Furukimi, *Effect of Nb on the proof strength of ferritic stainless steels at elevated temperatures.* ISIJ international, 2002. **42**(8): p. 916-920.
8. Fujita, N., et al., *Effect of Nb on high-temperature properties for ferritic stainless steel.* Scripta Materialia, 1996. **35**(6): p. 705-710.
9. Nakamura S., Miyakusu K., and Uematsu Y., CAMP-ISIJ, 1991. **4**: p. 1788-1791.
10. Oku M., et al., *Nissin Steel Technical Report*, 1996. p. 26-36.
11. Sim, G.M., et al., *Effect of Nb precipitate coarsening on the high temperature strength in Nb containing ferritic stainless steels.* Materials Science and Engineering: A, 2005. **396**(1–2): p. 159-165.
12. Morris, D.G., M.A. Muñoz-Morris, and C. Baudin, *The high-temperature strength of some Fe3Al alloys.* Acta Materialia, 2004. **52**(9): p. 2827-2836.
13. Fujita, N., K. Ohmura, and A. Yamamoto, *Changes of microstructures and high temperature properties during high temperature service of Niobium added ferritic stainless steels.* Materials science & engineering. A, Structural materials: properties, microstructure and processing, 2003. **351**(1-2): p. 272-281.
14. Sawatani, T., S. Minamino, and H. Morikawa, *Effect Of Laves Phase On The Properties Of Ti And Nb Stabilized Low C, N-19-Percent Cr-2-Percent Mo Stainless-Steel Sheets.* Transactions of the Iron and Steel Institute of Japan, 1982. **22**(3): p. 172-180.

15. Murata, Y., et al., *Dependence of Solvus Temperature of the Laves Phase on (Mo W Re) Contents in High Cr Ferritic Steels.* ISIJ international, 2005. **45**(1): p. 101-106.
16. Yan, H., et al., *Precipitation and mechanical properties of Nb-modified ferritic stainless steel during isothermal aging.* Materials Characterization, 2009. **60**(3): p. 204-209.
17. Narita, K., Journal of Japan Institute of Metallurgy, 1972. **11**: p. 49-57.
18. Jones, R.H., V.F. Zackay, and E.R. Parker, Metallurgical Transaction, 1972. **3**: p. 2835.
19. Borquez, O.P., *Investigations on diffusion-controlled transformations in creep resistant steels and graded cemented carbides*, in *der Fakultat fur Maschinenbau*2011, der Ruhr-Universitat Bochum.
20. Lifshitz, I.M. and V.V. Slyozov, *The kinetics of precipitation from supersaturated solid solutions.* Journal of Physics and Chemistry of Solids, 1961. **19**(1–2): p. 35-50.
21. Wagner, C., *Theorie der Alterung von Niederschlägen durch Umlösen (Ostwald-Reifung)" [Theory of the aging of precipitates by dissolution-reprecipitation (Ostwald ripening)]*. Zeitschrift für Elektrochemie, 1961. **65**(7): p. 581-591.
22. Humphreys, F.J. and M. Hatherly, *Recrystallization and related annealing phenomena*1995, Oxford, OX, UK; Tarrytown, N.Y., U.S.A.: Pergamon.
23. Michalak J.T. and Paxton H.W., Trans. Metall. Soc. A.I.M.E., 1961. **221**: p. 850.
24. Maki, T., *Principle and Various Methods for Grain Refinement of Steels.* CAMP-ISIJ, 2006. **19**: p. 410.
25. Shan Y. T., et al., *Mechganisms of Solidification Structure Improvement of Ultra Pure 17wt% Cr Ferritic Stainless Steel by Ti, Nb Addition.* Journal of Materials Science and Technology, 2011. **27**(4): p. 352-358.
26. Suehiro, M., *Recrystallization and Related Phenomena. An Analysis of the Solute Drag Effect of Nb on Recrystallization of Ultra Low Carbon Steel.* ISIJ international, 1998. **38**(6): p. 547-552.

27. Suehiro, M., Z.K. Liu, and J. Ågren, *Effect of niobium on massive transformation in ultra low carbon steels: a solute drag treatment.* Acta Materialia, 1996. **44**(10): p. 4241-4251.
28. Schmitt, J.H., *Some examples of stainless steel use in the automotive industry*, 2002, TRANS TECH PUBLICATIONS LTD. p. 17-22.
29. Cahn, J.W., *The impurity-drag effect in grain boundary motion.* Acta Metallurgica, 1962. **10**(9): p. 789-798.
30. Williams, D.B. and C.B. Carter, *Transmission Electron Microscopy*1996, New York: Plenum Press.
31. Miyazaki A., Yokota T., and T. F., *Hot-rolled ferritic steel for motor vehicle exhaust members*, U.S. Patent, Editor 11 August 1998.
32. Tsuzaki, K., et al., *High-Strain Rate Superplasticity And Role Of Dynamic Recrystallization In A Superplastic Duplex Stainless-Steel.* Materials transactions. JIM, 1990. **31**(11): p. 983-994.

APPENDIX A: MICROSTRUCTURAL ANALYSIS OF LAVES PHASE PRECIPITATES AND DISLOCATION DENSITY

Table A.1. Microstructural analysis of Laves phase precipitates and dislocation density

Sample	Time (sec)	Strain (%)	Volume fraction of Laves phase, v_f, (%)	Average size of Laves phase, r (nm)	Inter particle spacing , (nm) $\lambda = \frac{4(1-v_f)r}{3v_f}$	Dislocation density, ρ (nm^{-2})	Shape description of Laves phase
Unaged	60	0.3	4.88	22	572	1.77×10^{-5}	Mostly globular
	180	0.9	6.12	130	2659	5.02×10^{-6}	Mostly globular
	600	3.0	5.83	155	3338	6.29×10^{-6}	Mostly globular
	60	-	0.63	29	6099	5.26×10^{-6}	Mostly globular
	2860	-	4.61	92	2538	5.10×10^{-6}	Mostly globular
Aged	60	0.3	4.58	412	11445	tangles	Mostly rod-like
	600	3.0	4.43	402	11563	2.31×10^{-6}	Mostly rod-like
	2860	14.3	4.74	393	10531	3.62×10^{-6}	Mostly rod-like
	60	-	4.92	268	6906	2.23×10^{-6}	Mostly rod-like
	2860	-	5.35	313	7383	2.39×10^{-6}	Mostly rod-like

APPENDIX B: A PLOT OF DISLOCATION DENSITY VS. STRAIN

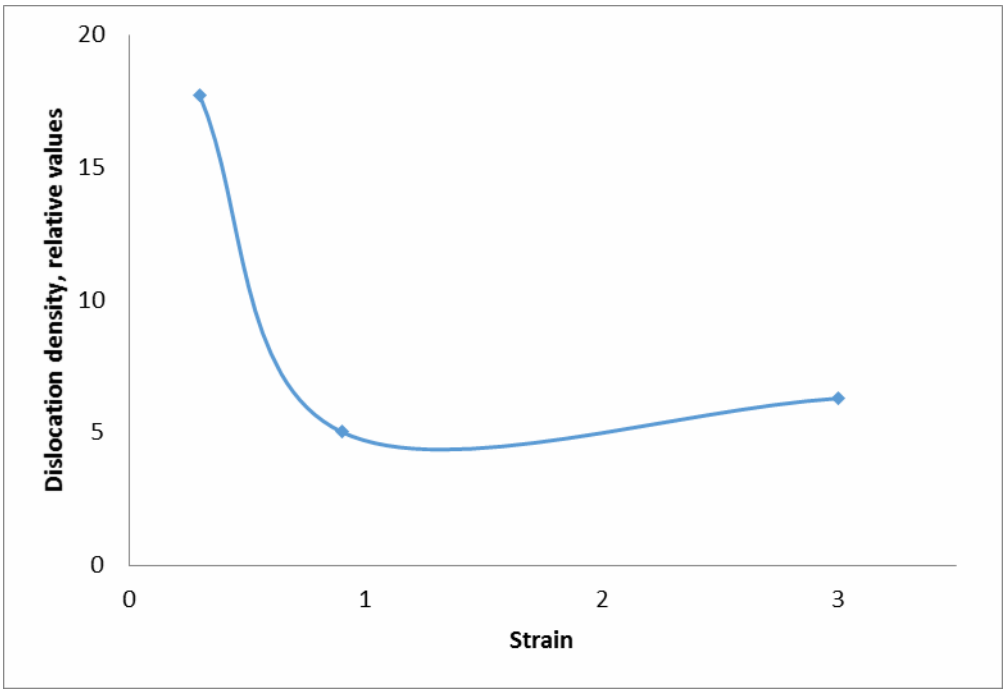

(a)

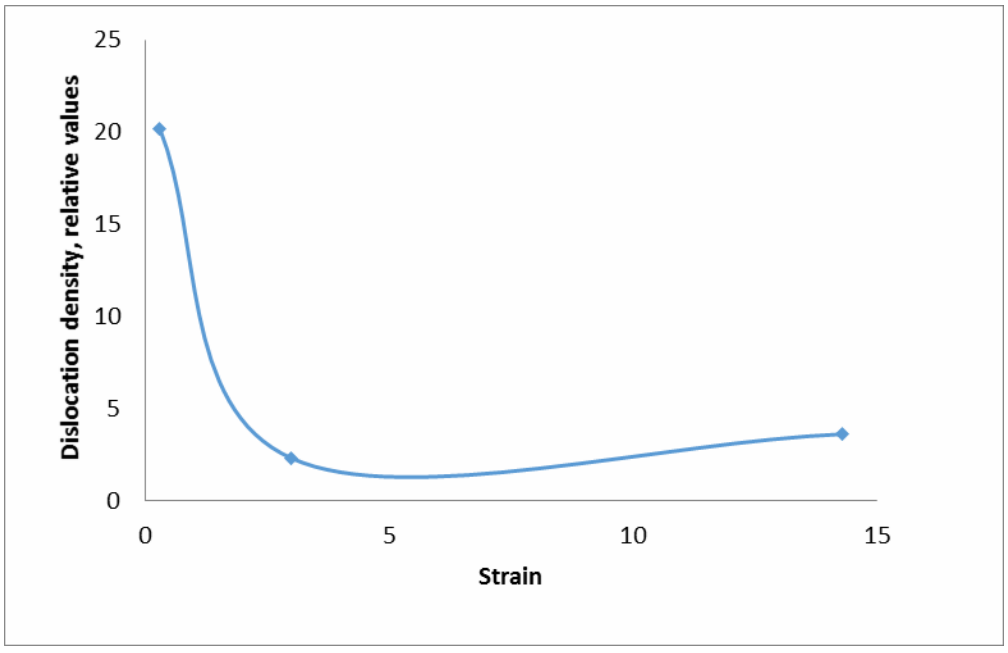

(b)

Figure B.1. A plot of dislocation density vs. strain (a) unaged (b) aged

APPENDIX C: A PLOT OF AVERAGE SIZE OF LAVES PHASE VS. STRAIN

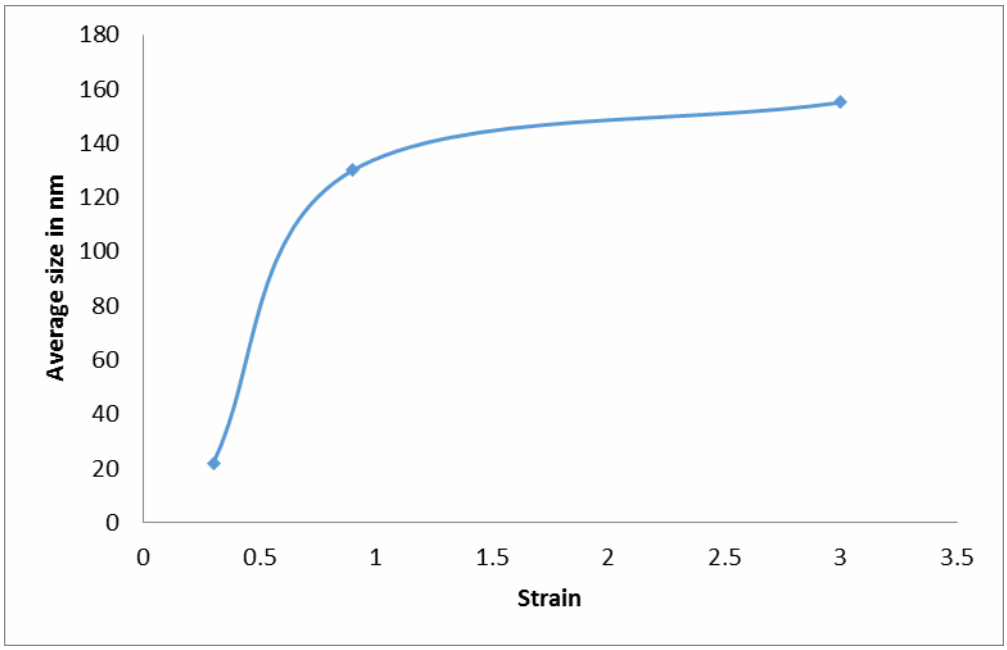

(a)

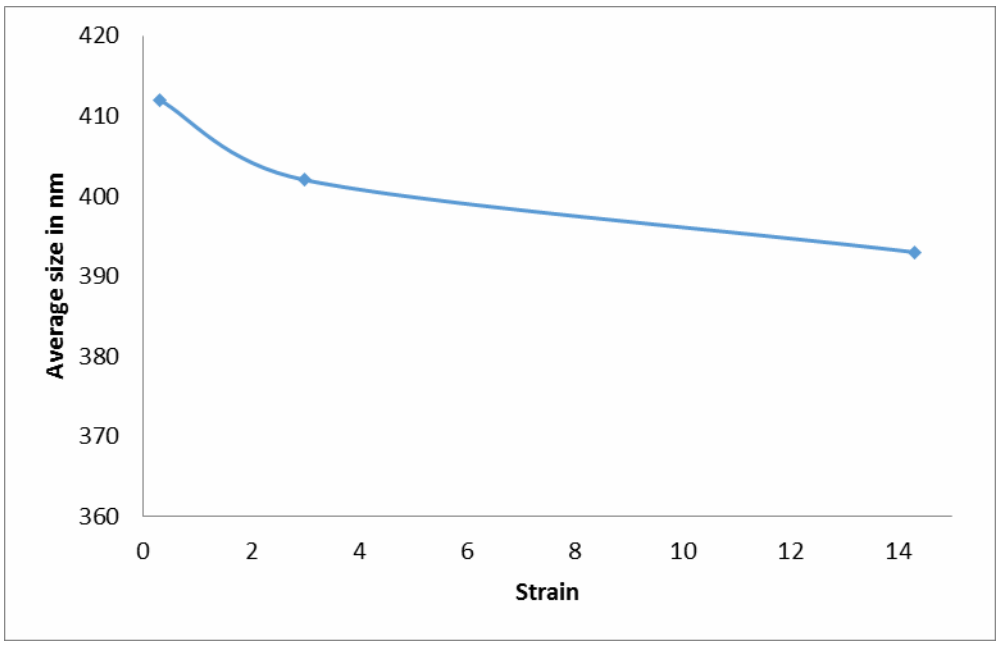

(b)

Figure C.1. A plot of average size of Laves phase vs. strain (a) unaged (b) aged

APPENDIX D: A PLOT OF VOLUME FRACTION OF LAVES PHASE VS. STRAIN

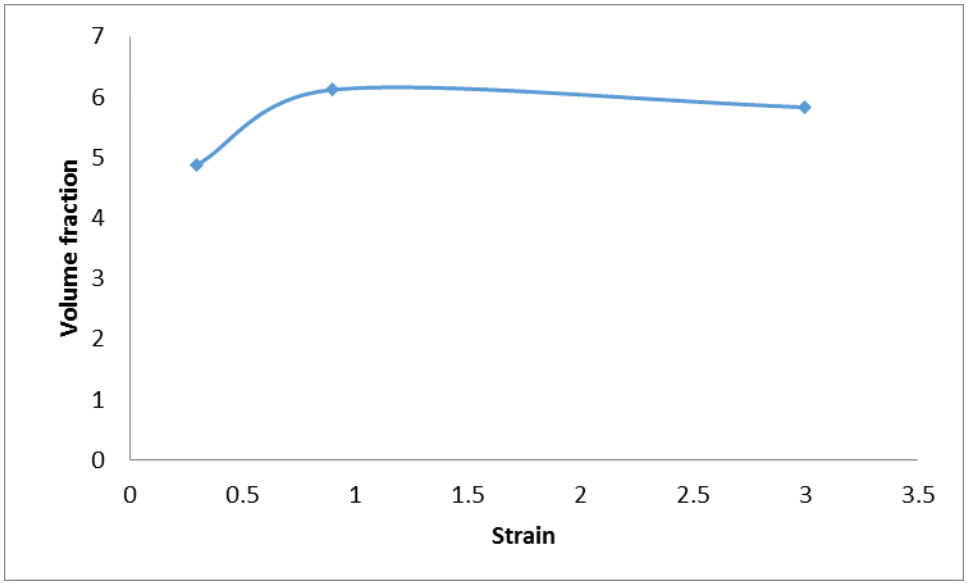

(a)

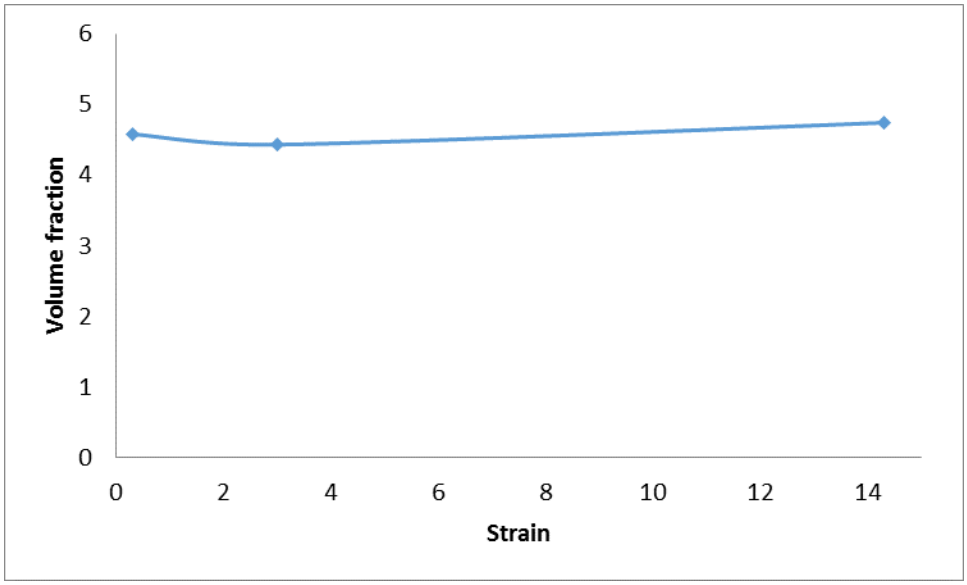

(b)

Figure D.1. A plot of volume fraction of Laves phase vs. strain (a) unaged (b) aged

APPENDIX E: A PLOT OF DISLOCATION DENSITY VS. TIME

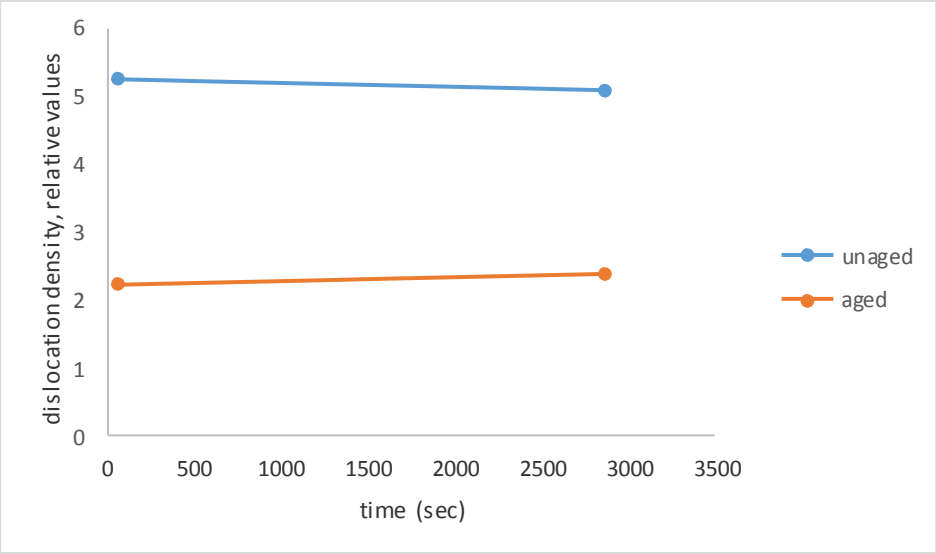

Figure E.1. A plot of dislocation density vs. time

APPENDIX F: A PLOT OF AVERAGE SIZE OF LAVES PHASES VS. TIME

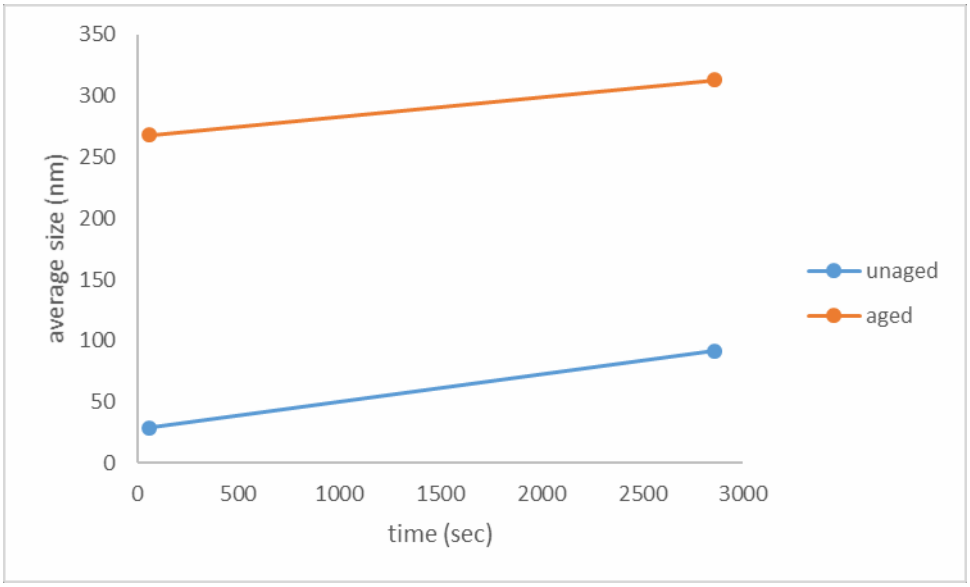

Figure F.1. A plot of average size of Laves phase vs. time

APPENDIX G: A PLOT OF VOLUME FRACTION OF LAVES PHASE VS. TIME

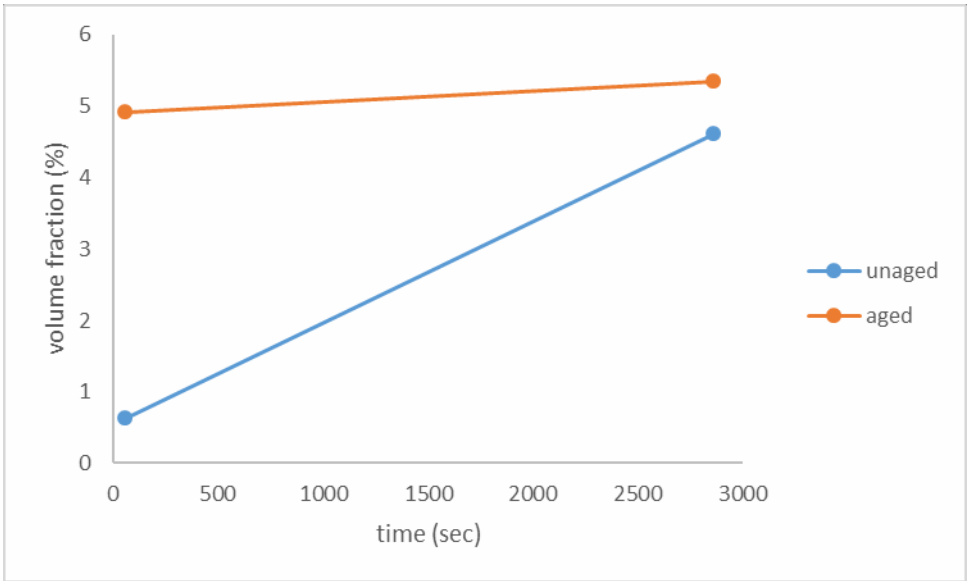

Figure G.1. A plot of volume fraction of Laves phase vs. time